Volume 1
Number 4
April 2022
Pages 179–240

Energy Advances

rsc.li/energy-advances

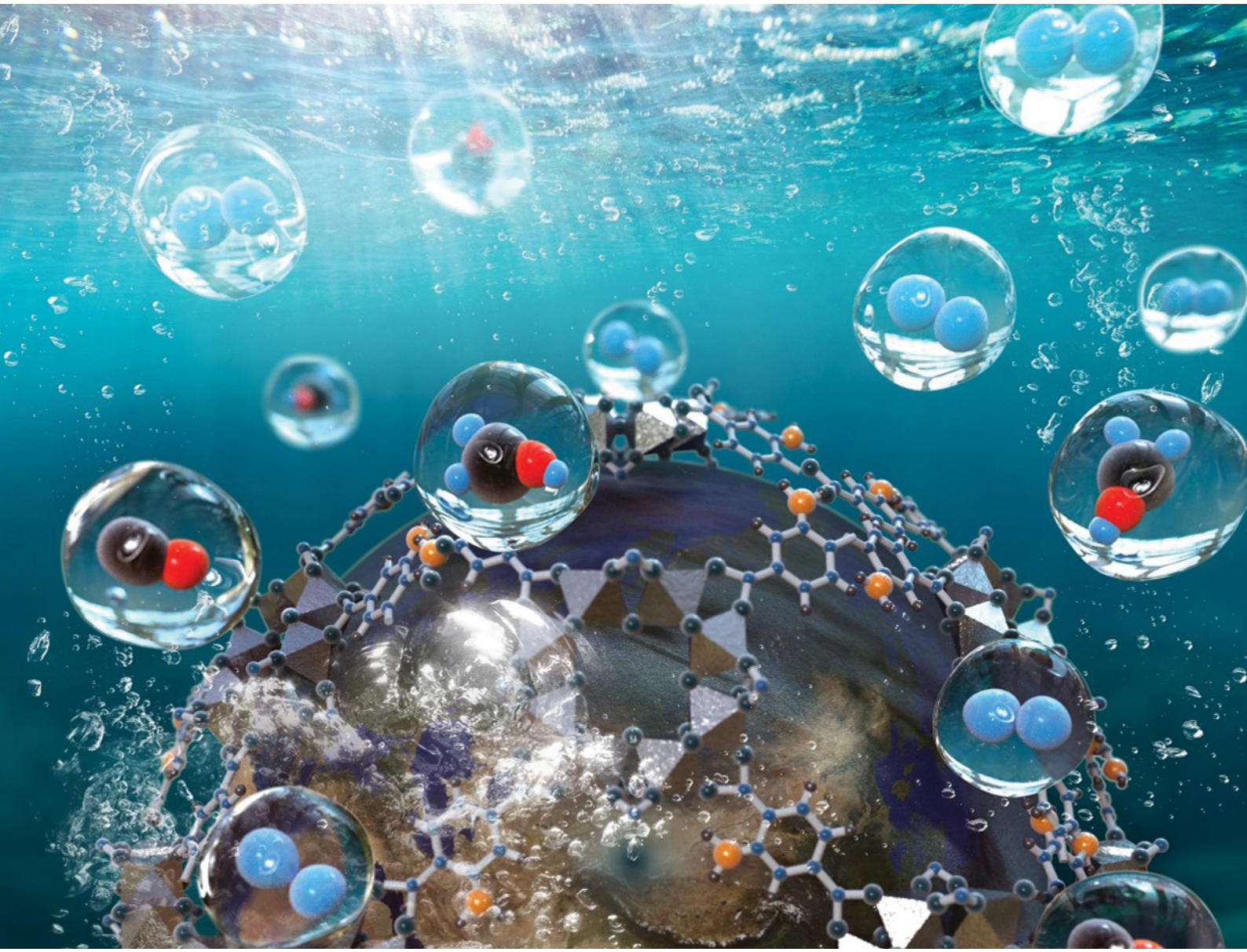

ISSN 2753-1457

ROYAL SOCIETY OF CHEMISTRY

PAPER

Jong-Heun Lee *et al.*

Type-II $BiVO_4/Ni_3$(hexahydroxytriphenylene)$_2$ heterojunction photoanodes for effective photoelectrochemical reaction

Energy Advances

ROYAL SOCIETY OF CHEMISTRY

PAPER

View Article Online
View Journal | View Issue

Cite this: *Energy Adv.*, 2022, 1, 197

Type-II $BiVO_4/Ni_3$(hexahydroxytriphenylene)$_2$ heterojunction photoanodes for effective photoelectrochemical reaction†

Ji Won Yoon, Young-Moo Jo and Jong-Heun Lee *

Semiconducting M_3(hexahydroxytriphenylene)$_2$ (M = Ni, Co, Cu; hexahydroxytriphenylene (HHTP)) was uniformly coated onto $BiVO_4$ thin films *via* a facile solvothermal process, and the photoelectrochemical performance of the $BiVO_4/M_3(HHTP)_2$ photoanodes was investigated. All three $BiVO_4/M_3(HHTP)_2$ photoanodes exhibited higher photocurrent densities than pristine $BiVO_4$. This can be attributed to the formation of type-II heterojunctions, as confirmed by ultraviolet photoelectron spectroscopy (UPS) and ultraviolet-visible spectroscopy. $BiVO_4/Ni_3(HHTP)_2$ exhibited the highest photocurrent density of 4.66 mA cm^{-2} at 1.23 V *vs.* a reversible hydrogen electrode (RHE), an approximately 3.2-fold increase from that of pristine $BiVO_4$. The results suggest that the type of metal ion in $M_3(HHTP)_2$ affects the electrical conductivity, which significantly influences the charge transport kinetics in the photoelectrochemical reactions of $BiVO_4$. The mechanism underlying the enhanced photoelectrochemical reaction was also investigated.

Received 15th January 2022,
Accepted 8th March 2022

DOI: 10.1039/d2ya00008c

rsc.li/energy-advances

Introduction

Hydrogen fuel is a sustainable energy source that can be used as an alternative to fossil fuels. Photoelectrochemical water splitting is an environment-friendly method to produce hydrogen from water by utilizing solar energy. This method has drawn significant attention owing to its potential for negligible greenhouse gas emissions. Among the diverse metal oxide photoanodes used for photoelectrochemical water splitting,[1,2] $BiVO_4$ is a promising candidate because of its 2.4–2.5 eV bandgap, which is advantageous for absorbing visible light. However, its sluggish charge transfer kinetics and short hole diffusion length hamper charge transport and separation.[3] Accordingly, various methods have been considered to improve the photoelectrochemical performance of $BiVO_4$, including surface area expansion, doping, and heterostructure design.[4–8]

The rational design of a type-II heterojunction with another semiconductor is a promising strategy to enhance the photoelectrochemical performance of $BiVO_4$.[9–12] A type-II heterojunction established between two different semiconductors facilitates the separation of photogenerated charge carriers, preventing charge recombination losses. Because a staggered band alignment is required, it is important to consider both the energy bandgap and band positions of the two semiconductors. The light absorption rate is determined by the energy bandgap, oxygen evolution reaction (OER), or hydrogen evolution reaction (HER) based on the band positions. Various heterostructures with staggered band alignments have been proposed to compensate for the sluggish OER, such as $WO_3/BiVO_4$,[5] $TiO_2/BiVO_4$,[6] and $BiVO_4/MoS_2$;[7] however, further enhancement of the photoelectrochemical performance is required.

In recent years, heterojunctions between metal–organic frameworks (MOFs) and $BiVO_4$, such as $BiVO_4$/CoNi–MOF,[13] $BiVO_4$/MIL-53(Fe),[14] and $BiVO_4$/MIL-101(Fe),[15] have been investigated to improve the photoelectrochemical performance. The design and application of MOFs for photoelectrochemical reactions have been widely investigated because MOFs provide advantages such as extremely high surface area, tunable porosity, and compositional diversity and exhibit semiconducting properties. Semiconducting MOFs with suitable band structures and high electrical conductivity are promising platforms for designing photoanodes with staggered band alignments.[16] Among various MOFs, $M_3(HHTP)_2$ (M = Ni, Co, and Cu; 2,3,6,7,10,11-hexahydroxytriphenylene (HHTP)) has shown good electrical conduction through π–π stacked pathways as well as suitable bandgaps for water splitting.[17] Because of their conductive nature, $M_3(HHTP)_2$ photoanodes are expected to exhibit high photoelectrochemical performance. However, to the best of our knowledge, the heterojunction between $BiVO_4$ and $M_3(HHTP)_2$ for photoelectrochemical reactions has yet to be investigated.

Department of Materials Science and Engineering, Korea University, Seoul 02841, Republic of Korea. E-mail: jongheun@korea.ac.kr

† Electronic supplementary information (ESI) available. See DOI: 10.1039/d2ya00008c

Herein, we report the highly efficient photoelectrochemical reaction of a $BiVO_4/M_3(HHTP)_2$ photoanode. The $BiVO_4$ film was coated onto fluorine doped tin oxide (FTO)/glass substrates by electrodeposition, then the $M_3(HHTP)_2$ was coated onto the $BiVO_4$ film *via* a solvothermal reaction. All $BiVO_4/M_3(HHTP)_2$ photoanodes showed significantly higher photocurrent densities than pristine $BiVO_4$, which is attributed to the type-II heterojunctions established between $BiVO_4$ and $M_3(HHTP)_2$. Notably, $BiVO_4/Ni_3(HHTP)_2$ exhibited the highest photocurrent density of 4.66 mA cm^{-2}, which is a 3.2-fold increase in efficiency from that of pristine $BiVO_4$. This study reveals that the electrical conductivity of $M_3(HHTP)_2$ is dependent on the type of metal ions, which play a key role in the charge transport for photoelectrochemical reactions. The main purpose of this study is to determine the key parameters affecting the OER in $BiVO_4/M_3(HHTP)_2$ heterostructure photoanodes and to understand the mechanism underlying the enhanced photoelectrochemical reaction.

Experimental

Sample preparation

$BiVO_4$ nanoparticles were coated onto FTO/glass substrates by a modified electrodeposition method.[18,19] The typical synthesis process includes an FTO/glass substrate, platinum (Pt) mesh, and Ag/AgCl/saturated NaCl as the working, counter, and reference electrodes, respectively. The precursor solution for $BiVO_4$ electrodeposition was prepared as follows. 1.141 g of vanadium oxide sulfate hydrate ($VOSO_4{\cdot}xH_2O$, 99.9%, Alfa Aesar), and 0.97014 g of bismuth nitrate pentahydrate ($Bi(NO_3)_3{\cdot}5H_2O$, 98.0%, Junsei) were dissolved in an aqueous HNO_3 solution (100 mL, 1 : 9 (v/v) mixture of 60% HNO_3 and deionized (DI) water) under magnetic stirring to form a clear solution. A stabilizer solution was prepared by dissolving 32.812 g of sodium acetate in 100 mL of DI water, and then added to the Bi/V ion solution. The pH of the solution for electrodeposition was adjusted to 4.7. This mildly acidic pH solution is required for electrodeposition because no film can be deposited at pH values, in which Bi ions are soluble (pH $<$ 2). Excessive precipitates hinder the film deposition at pH $>$ 5.[19] Electrodeposition was performed at 0.8 V for 1 h at room temperature. The prepared substrates were rinsed with DI water and annealed at 550 °C for 3 h.

$Ni_3(HHTP)_2$ was coated onto the $BiVO_4$ film *via* a solvothermal reaction. 2.5 mmol of nickel acetate tetrahydrate ($Ni(OCOCH_3)_2{\cdot}4H_2O$, 98.0%, Merck) was dissolved in 20 mL of DI water, and 1.25 mmol of 2,3,6,7,10,11-hexahydroxytriphenylene (HHTP, 95.0%, Acros Organics) was dissolved in 10 mL methanol. The two solutions were mixed and homogenized by stirring. Then, the mixed solution was placed in a Teflon-lined stainless-steel autoclave with a $BiVO_4$/FTO/glass substrate immersed in it. The sealed autoclave was heated to 85 °C for 3.5 h. The substrates were rinsed with DI water thrice.

Results & discussion

A schematic of the procedure for preparing the $BiVO_4/Ni_3(HHTP)_2$ heterojunction on an FTO/glass substrate is shown in Fig. 1. The $BiVO_4$ thin film was anodically electrodeposited onto the FTO/glass substrate using an aqueous solution containing Bi(III) ions and V(IV) ions. This was followed by heat treatment at 500 °C for 2 h to achieve crystalline $BiVO_4$. The

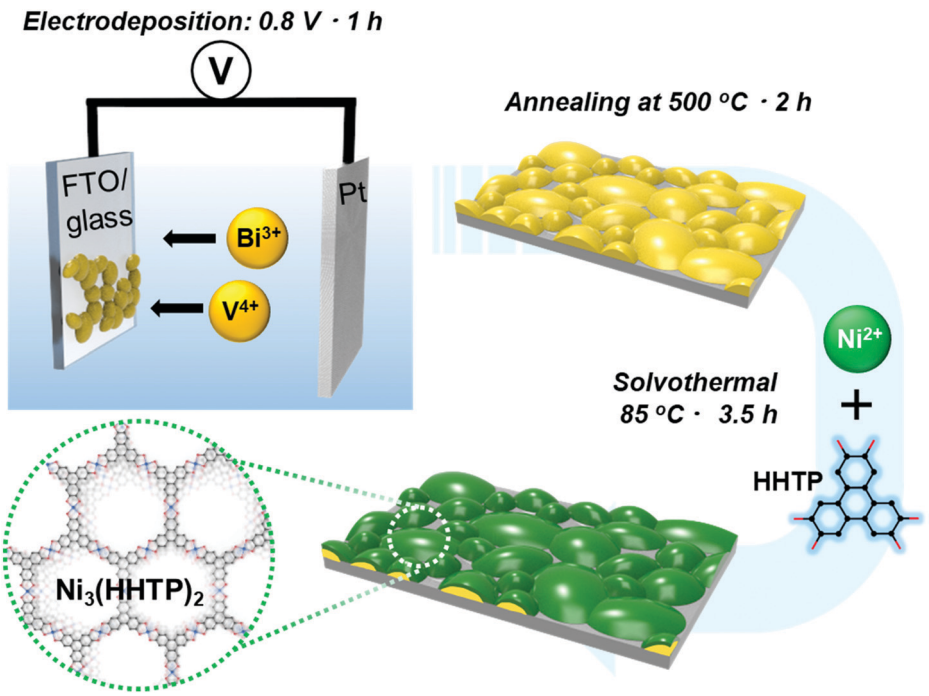

Fig. 1 Schematic diagram of the synthesis process for the $BiVO_4/Ni_3(HHTP)_2$ heterostructure on FTO/glass substrate.

$BiVO_4$ thin film appeared as bright yellow (Fig. S1a, ESI†). The X-ray diffraction (XRD) pattern showed that the crystalline peaks are monoclinic $BiVO_4$ (Fig. S1b, ESI†). The scanning electron microscopy (SEM) images of the $BiVO_4$ thin film (Fig. S2a and b, ESI†) revealed that the film consists of large grains ranging from 100 to 500 nm with a thickness of 250–300 nm. The transmission electron microscopy (TEM) image and selected area electron diffraction (SAED) patterns of $BiVO_4$ confirmed its crystalline structure. The inter-planar spacing in the lattice fringes was analyzed to be $d_{(040)}$ = 2.90 ± 0.1 Å (Fig. S2c, ESI†), which corresponds to the monoclinic $BiVO_4$. Elemental mapping further confirmed that the Bi and V components were uniformly distributed along the whole grains (Fig. S2(d1)–S4, ESI†).

$Ni_3(HHTP)_2$ was coated onto the surface of $BiVO_4$ by a solvothermal reaction at 85 °C for 3.5 h (Fig. 2a and b). The solvothermal reaction enables the conformal, well-attached, and uniform growth of $Ni_3(HHTP)_2$ on the $BiVO_4$ surface. This is desirable in photoelectrochemical reactions because the strong adhesion between the $BiVO_4$ and MOF ensures high stability. The color of the photoanode changed from bright yellow to dark green after the solvothermal growth of $Ni_3(HHTP)_2$ on the $BiVO_4$ thin film (Fig. 2c). Close examination of the high-resolution TEM (Fig. 2d) and elemental mapping (Fig. 2e1–6) confirmed that the $Ni_3(HHTP)_2$ layer (150–200 nm thickness) was uniformly coated onto the $BiVO_4$ surface. Owing to the XRD detection limit and the negligible number of MOFs, $Ni_3(HHTP)_2$ peaks were not observed in the XRD patterns (Fig. S3a, ESI†). To prepare a sufficient amount of $Ni_3(HHTP)_2$, the solvothermal reaction time was increased to 6 h. The detected peaks of MOF at 2θ = 5–20° were in agreement with those observed in the simulated XRD patterns of $Ni_3(HHTP)_2$ (Fig. S3b, ESI†), confirming the formation of $Ni_3(HHTP)_2$ *via* the solvothermal reaction.[20–22] Furthermore, the atomic composition of the $BiVO_4/M_3(HHTP)_2$ (M = Ni, Co, Cu) was analyzed by XPS (Fig. S4–S6, ESI†), and the existence of all the elements was confirmed by peak analysis. To examine the influence of the solvothermal reaction time on the growth of $Ni_3(HHTP)_2$ on the $BiVO_4$ surface, the reaction time was controlled up to 1 h and 6 h. As the MOF precursor solution containing nickel ions and HHTP ligands induced rapid nucleation and growth at the initial stage, the morphology of $Ni_3(HHTP)_2$ after the 1 h and 3.5 h solvothermal reactions appeared to be similar (Fig. S7a, b, ESI† and Fig. 2a, b). However, when the solvothermal reaction time increased to 6 h, a thick $Ni_3(HHTP)_2$ layer (4–5 μm) unevenly covered the $BiVO_4$ film (Fig. S7c and d, ESI†). An excessively thick $Ni_3(HHTP)_2$ layer will affect the charge transfer within the $Ni_3(HHTP)_2$, which would deteriorate photoelectrochemical reaction. Hence, the thickness of $Ni_3(HHTP)_2$ should be optimized by controlling the solvothermal reaction time.

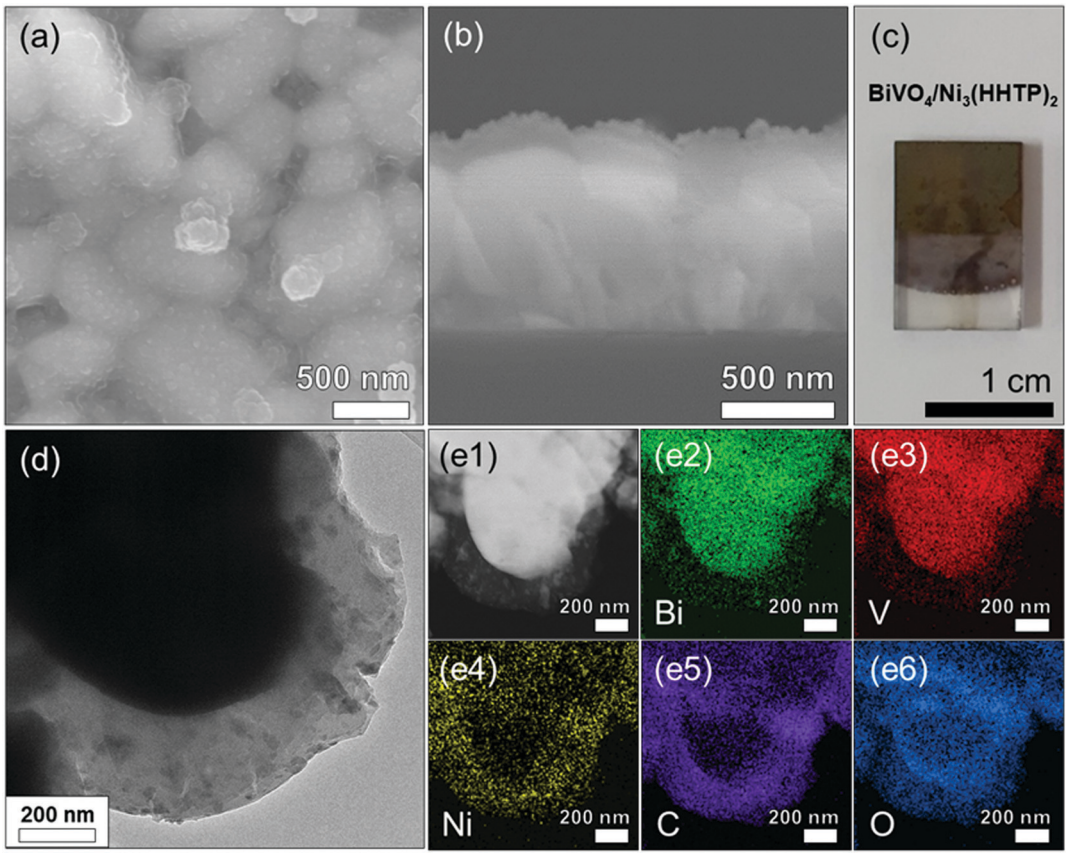

Fig. 2 (a) Top-view and (b) cross-sectional view of the SEM image of $BiVO_4/Ni_3(HHTP)_2$ heterostructure (solvothermal reaction for 3.5 h). (c) Photograph of $BiVO_4/Ni_3(HHTP)_2$ heterostructure photoanode. (d) TEM image and (e1–6) elemental mappings of $BiVO_4/Ni_3(HHTP)_2$ heterostructure.

The photocurrent densities of $BiVO_4$ and $BiVO_4/Ni_3(HHTP)_2$ were evaluated in both 0.1 M Na_2SO_3 and 0.1 M Na_2SO_4 solution under front and back illumination (Fig. 3a). In $BiVO_4$ photoanodes with sluggish charge transport kinetics, backside illumination led to a higher photocurrent density than frontside illumination because it allows the more efficient collection of photogenerated electrons.[23,24] In the present study, hole-scavenging Na_2SO_3 was used to suppress the surface recombination of $BiVO_4$.[25] At the potential of 1.23 V *vs.* RHE, $BiVO_4$ under front and back illumination showed photocurrent densities of 1.09 mA cm^{-2} and 1.42 mA cm^{-2}, respectively. When $Ni_3(HHTP)_2$ was solvothermally coated onto $BiVO_4$ for 3.5 h, the photocurrent density significantly increased to 3.45 and 4.66 mA cm^{-2} under front and back illumination, respectively, which is approximately 3.2 times higher than that of a pristine $BiVO_4$ photoanode. When the solvothermal reaction time reached 6 h, however, the photocurrent density of $BiVO_4/Ni_3(HHTP)_2$ significantly decreased, probably because of ineffective charge transport through the extremely thick MOF layer (Fig. S8, ESI†). The photocurrent density of $BiVO_4/Ni_3(HHTP)_2$ reached 3.10 mA cm^{-2} at 1.23 V *vs.* RHE in 0.1 M Na_2SO_4 electrolyte (without hole-scavenging Na_2SO_3), suggesting that $Ni_3(HHTP)_2$ is also a promising catalyst for photoelectrochemical water splitting (Fig. S9, ESI†). It is worth noting that the photocurrent density of the $BiVO_4/Ni_3(HHTP)_2$ photoanode is similar to or greater than that of previous $BiVO_4$-based heterojunction photoanodes in the literature (Table S1, ESI†). Besides, $BiVO_4/Ni_3(HHTP)_2$ showed an abrupt slope change above 1.1 V *vs.* RHE with or without the presence of Na_2SO_3. The *J*–*V* curves shown in Fig. S10 (ESI†) revealed that the current density of $BiVO_4$ did not significantly increase in the dark, while $Ni_3(HHTP)_2$ and $BiVO_4/Ni_3(HHTP)_2$ have a different increasing trend above 1.1 V *vs.* RHE. Therefore, the unusual increasing trend could be attributed to an intrinsic catalytic activity of $Ni_3(HHTP)_2$. The light on/off cycles of $BiVO_4$ and $BiVO_4/Ni_3(HHTP)_2$ were obtained by applying the constant potential of 1.23 V *vs.* RHE (Fig. 3b). Both photoanodes exhibited rapid photoresponses under initial illumination, followed by a stable steady-state, and were highly reproducible for a few cycles. The incident photon-to-electron conversion efficiency (IPCE) spectra were examined from 300 to 800 nm at 1.23 V *vs.* RHE to investigate the light absorption and energy conversion efficiency of $BiVO_4$ and $BiVO_4/Ni_3(HHTP)_2$ (Fig. 3c). $BiVO_4/Ni_3(HHTP)_2$ reached the highest IPCE of 83.4% at λ = 460 nm, which is almost four times higher than that of pristine $BiVO_4$. The IPCE value significantly increased throughout the entire range, indicating that $Ni_3(HHTP)_2$ promoted the effective utilization of visible light. Electrochemical impedance spectroscopy (EIS) of $BiVO_4$ and $BiVO_4/Ni_3(HHTP)_2$ was conducted at 1.23 V *vs.* RHE to examine the surface resistance and charge transport

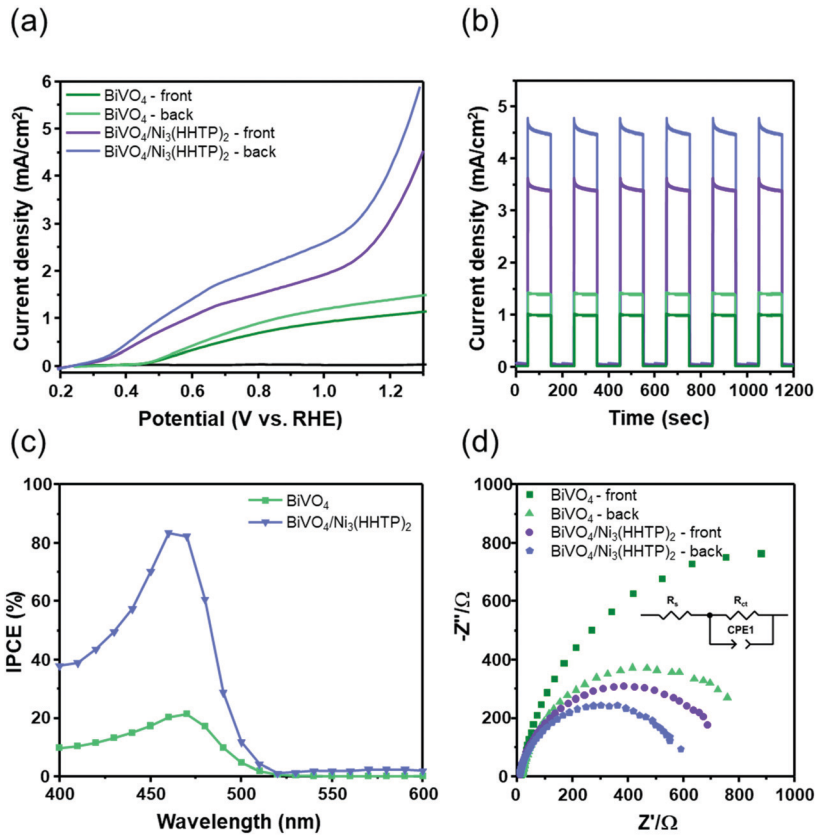

Fig. 3 (a) *J*–*V* curves of $BiVO_4$ and $BiVO_4/Ni_3(HHTP)_2$ (front and back illumination) in a 0.1 M Na_2SO_3 electrolyte. (b) Light on/off current density transients of $BiVO_4$ and $BiVO_4/Ni_3(HHTP)_2$ (front and back illumination) at 1.23 V *vs.* RHE. (c) IPCE measurements of $BiVO_4$ and $BiVO_4/Ni_3(HHTP)_2$. (d) EIS analysis for $BiVO_4$ and $BiVO_4/Ni_3(HHTP)_2$ (front and back illumination).

Table 1 Fitted charge transfer resistance

Photoanode	R_s (Ω cm^2)	R_{ct} (Ω cm^2)
$BiVO_4$ (front)	17.3	1740
$BiVO_4$ (back)	17.7	909.5
$BiVO_4/Ni_3(HHTP)_2$ (front)	8.5	665.3
$BiVO_4/Ni_3(HHTP)_2$ (back)	7.4	447.9

during photoelectrochemical reactions (Fig. 3d). The obtained Nyquist plots were fitted and simulated to determine the R_{ct} values (charge transfer resistance at the interface between the photoanode and electrolyte) listed in Table 1. An equivalent circuit for the EIS results is shown in the inset of Fig. 3d. According to the fitted charge transfer resistance, back-illuminated $BiVO_4$ and $BiVO_4/Ni_3(HHTP)_2$ exhibited lower resistance than front-illuminated photoanodes. The results indicate that backside illumination is advantageous for collecting photogenerated electrons and can overcome the sluggish charge transport kinetics of $BiVO_4$. Moreover, additional EIS measurements (Fig. S11a, ESI†) were conducted in the dark at 0 V to confirm a junction formed between $BiVO_4$ and $Ni_3(HHTP)_2$. Without any external bias and light energy, the EIS spectra of $BiVO_4$ revealed one semicircle, while $BiVO_4/Ni_3(HHTP)_2$ revealed two semicircles. When $Ni_3(HHTP)_2$ formed a junction with $BiVO_4$, the R_{ct} values decreased from 909.5 Ω cm^2 to 447.9 Ω cm^2, indicating a facilitated charge transfer through the $BiVO_4/Ni_3(HHTP)_2$ and electrolyte interface. In addition, the charge carrier concentration (N_D) was calculated using Mott–Schottky analysis (Fig. S11b, ESI†). According to the Mott–Schottky plot, N_D can be calculated using the following equation:[26]

$$N_D = \frac{2}{e\varepsilon_0\varepsilon} \times \left[\frac{d\left[\frac{1}{C^2}\right]}{dV_s}\right]^{-1}, \quad (1)$$

where e is the electronic charge (1.6×10^{-19} C), ε_0 is the vacuum permittivity (8.854×10^{-12} F m^{-1}), ε is the relative permittivity of $BiVO_4$ (68),[27] C (F cm^{-2}) is the space charge capacitance, and V_s (V) is the applied potential. The obtained N_D values for $BiVO_4$ and $BiVO_4/Ni_3(HHTP)_2$ were 1.86×10^{16} cm^{-3} and 3.03×10^{16} cm^{-3}, respectively. The results indicated that higher charge carrier concentration is generated through the heterojunction formed between $BiVO_4$ and $Ni_3(HHTP)_2$, implying that $Ni_3(HHTP)_2$ was highly effective at promoting charge carrier transport.

$Co_3(HHTP)_2$ and $Cu_3(HHTP)_2$ are two other potential conductive MOFs[28] that were coated onto $BiVO_4$ by a solvothermal reaction to investigate their photoelectrochemical performance. Upon their use, the photocurrent density increased to 2.25 and 1.77 mA cm^{-2} (Fig. S12a, ESI†). The IPCE values of $BiVO_4/Co_3(HHTP)_2$ and $BiVO_4/Cu_3(HHTP)_2$ were more than twice that of with pristine (Fig. S12b, ESI†). The fitted R_{ct} values decreased as $Co_3(HHTP)_2$ and $Cu_3(HHTP)_2$ were coated onto $BiVO_4$ (Fig. S12c, d and Table S2, ESI†). The results confirm that the formation of a heterostructure photoanode between semiconducting HHTP-based MOFs and $BiVO_4$ could enhance photoelectrochemical reactions.[29–33] Although $Co_3(HHTP)_2$ and $Cu_3(HHTP)_2$ improved the photoelectrochemical activity of $BiVO_4$, its efficiency was lower than that of $BiVO_4/Ni_3(HHTP)_2$. The higher electrochemical performance of $Ni_3(HHTP)_2$ can be understood in terms of its high electrical conductivity among the three HHTP-based MOFs. To examine this, porous $M_3(HHTP)_2$ pellets were prepared (Fig. S13a, ESI†), and their electrical conductivities were measured using the two-electrode method. The conductivities are $\sigma = 4.45 \times 10^{-6}$ S cm^{-1}, 1.59×10^{-7} S cm^{-1}, and 4.29×10^{-8} S cm^{-1} for $Ni_3(HHTP)_2$, $Co_3(HHTP)_2$, and $Cu_3(HHTP)_2$, respectively (Fig. S13b, ESI†). The conductivity of $Ni_3(HHTP)_2$ is significantly higher than those of $Co_3(HHTP)_2$ and $Cu_3(HHTP)_2$, even considering the small variation in densities, which is in line with the reported results.[17] For $M_3(HHTP)_2$, the electrical conductivity is dependent on the type of metal ion with different electronic states.[34] Moreover, as $M_3(HHTP)_2$ frameworks are built in stacked two-dimensional (2D) structures, the interlayer spacing (S) along the c direction also influences the conduction. In general, a higher S value with a lower strength of interaction between the 2D layers yields a higher conductivity.[35] In the literature, $Ni_3(HHTP)_2$ was reported to have the highest S value (3.8 Å),[36] while $Cu_3(HHTP)_2$ had the lowest (3.16 Å) among the three MOFs.[17] The conductivity values in the present study and literature suggest that the high conductivity of $Ni_3(HHTP)_2$ plays a key role in the superior photoelectrochemical performance of the $BiVO_4/Ni_3(HHTP)_2$ photoanode.

To reveal the dynamics of light absorption, charge separation, and charge transfer, the intrinsic band structures of $BiVO_4$ and $Ni_3(HHTP)_2$ were investigated using ultraviolet photoelectron spectroscopy (UPS) and ultraviolet-visible (UV-vis) spectroscopy. Fig. 4a and b show the UPS of $BiVO_4$ and $Ni_3(HHTP)_2$ for obtaining the work function (ϕ, energy from vacuum level to Fermi level) and valence band maximum (VBM, energy from Fermi level to valence band maximum). The work functions of $BiVO_4$ and $Ni_3(HHTP)_2$ are 4.20 eV and 5.0 eV, while the VBM values are 2.25 eV and 1.62 eV, respectively. The UV-vis spectra in Fig. 4c shows that the energy bandgaps of $BiVO_4$ and $Ni_3(HHTP)_2$ were 2.50 and 2.68 eV, respectively. The intrinsic band structures of $BiVO_4$ and $Ni_3(HHTP)_2$ are shown in Fig. 4d. As $BiVO_4$ has a higher E_F than $Ni_3(HHTP)_2$, the electrons would transfer from $BiVO_4$ to $Ni_3(HHTP)_2$ until equilibrium is reached. After the electronic state reached equilibrium, the band structure caused the upward band edge bending of $BiVO_4$, and downward band edge bending of $Ni_3(HHTP)_2$, forming a type-II heterojunction. In the type-II heterojunction established in $BiVO_4/Ni_3(HHTP)_2$, the photogenerated electrons migrated from the conduction band (E_C) of $Ni_3(HHTP)_2$ to the E_C of $BiVO_4$. In contrast, the photogenerated holes migrated from the valence band (E_V) of $BiVO_4$ to the E_V of $Ni_3(HHTP)_2$, facilitating the separation of photogenerated charge carriers (Fig. 4e). In addition, the intrinsic band structures of $Co_3(HHTP)_2$ and $Cu_3(HHTP)_2$ were investigated to understand the band-bending between $BiVO_4/Co_3(HHTP)_2$ and $BiVO_4/Cu_3(HHTP)_2$ (Fig. S14 and S15, ESI†). Both $BiVO_4/Co_3(HHTP)_2$ and $BiVO_4/$

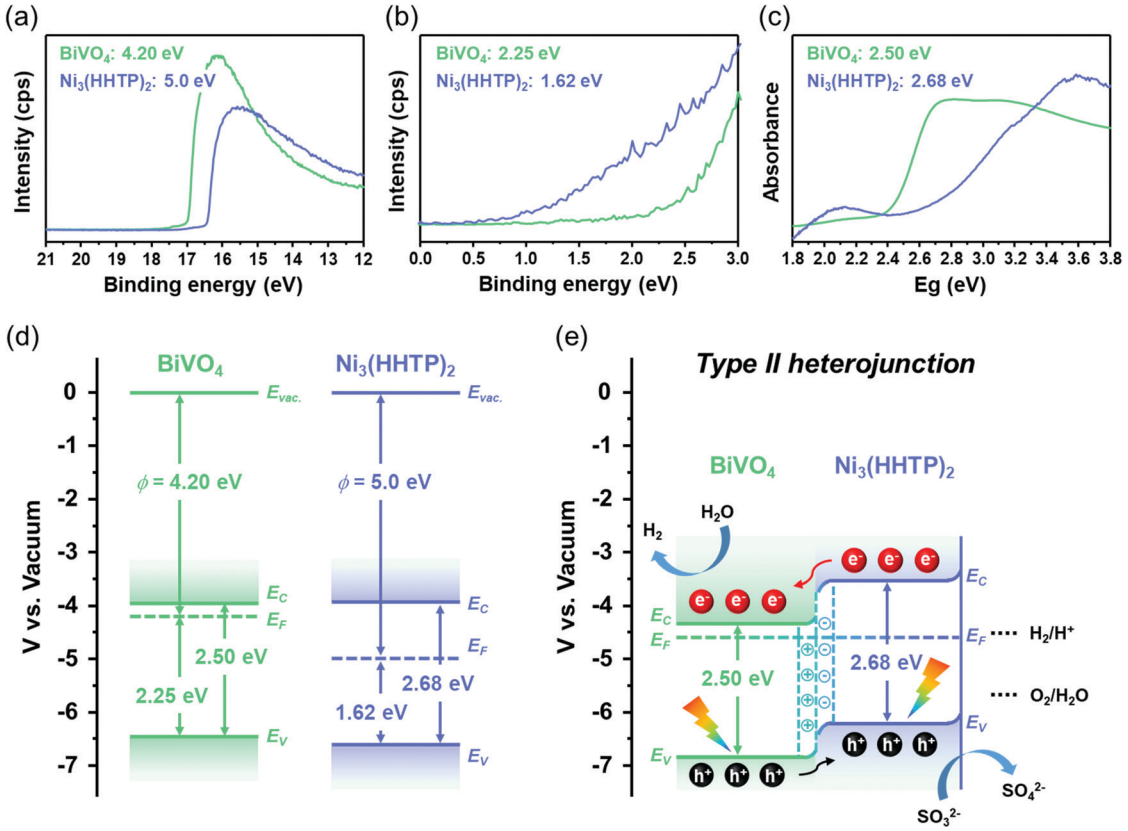

Fig. 4 UPS of $BiVO_4$ and $BiVO_4/Ni_3(HHTP)_2$ for obtaining (a) work function (ϕ) and (b) VBM. (c) UV-vis spectra of $BiVO_4$ and $BiVO_4/Ni_3(HHTP)_2$. Schematic energy band diagram of $BiVO_4$ and $BiVO_4/Ni_3(HHTP)_2$ (d) before contact and (e) after contact.

$Cu_3(HHTP)_2$ achieved the type-II heterojunction after reaching equilibrium. The band-bending structure is in line with the photoelectrochemical activities, indicating that the coating with HHTP-based MOFs promotes effective charge separation for the efficient photoelectrochemical performance of $BiVO_4$. The results validate the high versatility of HHTP-based MOFs along with the enhanced photoelectrochemical activities of $BiVO_4$/HHTP-based MOF heterostructure photoanodes.

Aside from band-bending diagrams of $BiVO_4/Ni_3(HHTP)_2$, it is crucial to examine the three critical factors affecting the photoelectrochemical activity: light absorption efficiency (η_{abs}), charge separation efficiency (η_{sep}), and charge transfer efficiency (η_{trans}). The three factors are expressed in the following water oxidation equation:[37–39]

$$J_{water} = J_{max} \times \eta_{abs} \times \eta_{sep} \times \eta_{trans} \quad (2)$$

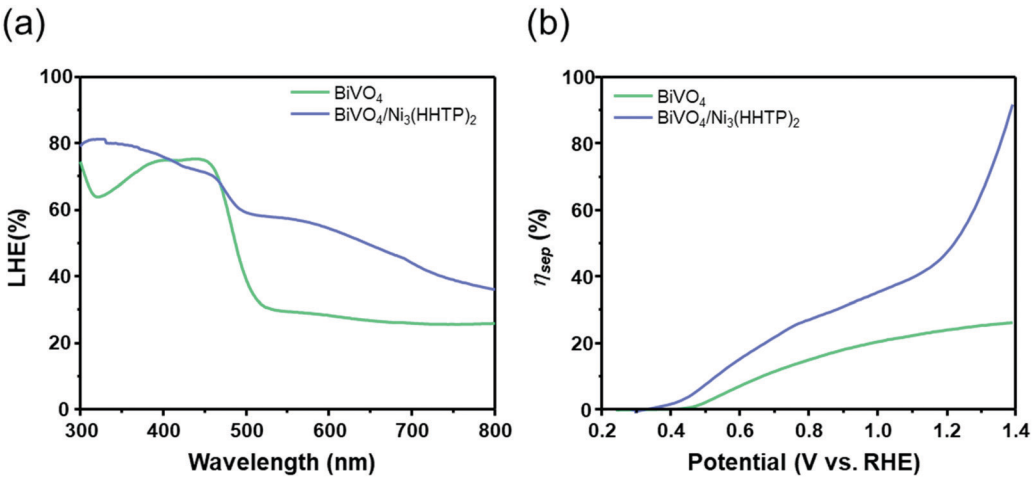

Fig. 5 (a) Light harvesting efficiency (LHE) (%) and (b) charge separation efficiency (η_{sep}) of $BiVO_4$ and $BiVO_4/Ni_3(HHTP)_2$.

where J_{max} is the theoretical maximum photocurrent density, and J_{water} is the experimentally obtained photocurrent density. To simplify the equation, η_{trans} can be assumed as 100% when the hole scavenger (Na_2SO_3) that induces rapid oxidation kinetics is present in the electrolyte.

$$J_{sulfite} = J_{max} \times \eta_{abs} \times \eta_{sep} \quad (3)$$

If it is assumed that all the absorbed photons are fully converted to photocurrent density, the η_{sep} and η_{trans} can be neglected. The equation can be further simplified as follows:

$$J_{abs} = J_{max} \times \eta_{abs} \quad (4)$$

Light absorption was observed at 496 nm and 504 nm for $BiVO_4$ and $BiVO_4/Ni_3(HHTP)_2$, respectively (Fig. 5a). By integrating the electron flux of both air mass (AM) 1.5G and the photoanode, as shown in Fig. S16a and b (ESI†), the J_{max} of $BiVO_4$ and $BiVO_4/Ni_3(HHTP)_2$ are 6.44 mA cm^{-2} and 6.95 mA cm^{-2}, while the J_{abs} are 4.42 mA cm^{-2} and 4.89 mA cm^{-2}, respectively (Table S3, ESI†). The η_{abs} of $BiVO_4$ and $BiVO_4/Ni_3(HHTP)_2$ were calculated as 68.6% and 70.4%, respectively. Although $BiVO_4/Ni_3(HHTP)_2$ yielded higher η_{abs} than $BiVO_4$, the enhancement was not significant because $Ni_3(HHTP)_2$ has a bandgap of 2.68 eV, which is slightly larger than that of $BiVO_4$ (2.50 eV). The $\eta_{abs} \times \eta_{sep}$ of $BiVO_4$ and $BiVO_4/Ni_3(HHTP)_2$ were obtained by eliminating the η_{trans} (Fig. S16c, ESI†). Consequently, with the known η_{abs}, the η_{sep} of the photoanodes was calculated, as shown in Fig. 5b. When $Ni_3(HHTP)_2$ was coated onto $BiVO_4$, the η_{sep} significantly increased to 51.4%, which is 2.1 times higher than that of pristine $BiVO_4$ film. These results show that establishing a type-II heterojunction between $Ni_3(HHTP)_2$ and $BiVO_4$ promotes effective charge separation, which ultimately improves the photoelectrochemical performance of the photoanodes. The long-term stability of the $BiVO_4$ and $BiVO_4/Ni_3(HHTP)_2$ photoanodes was also examined for 40 000 s at 1.23 V *vs.* RHE (Fig. S17, ESI†). No severe degradation was observed, and the results indicate that $BiVO_4/Ni_3(HHTP)_2$ was electrochemically stable over a long period. In addition, the structure of $BiVO_4/Ni_3(HHTP)_2$ after photoelectrochemical reactions was observed by TEM and elemental mappings (Fig. S18, ESI†). The adhesion between $BiVO_4$ and $Ni_3(HHTP)_2$ was strong enough to maintain its stable structure even after photoelectrochemical reactions.

Conclusions

$BiVO_4/M_3(HHTP)_2$ heterojunction photoanodes with three different metal ions (M = Ni, Co, and Cu) were prepared *via* facile electrodeposition followed by a solvothermal process for photoelectrochemical reactions. The $M_3(HHTP)_2$ coating is aimed at improving the sluggish charge transport kinetics of $BiVO_4$ by forming staggered band alignments. All three $BiVO_4/M_3(HHTP)_2$ photoanodes exhibited higher photocurrent densities than the pristine $BiVO_4$ film; type-II heterojunctions were observed between $BiVO_4$ and $M_3(HHTP)_2$. Effective light absorption and charge separation were achieved through the type-II heterojunctions, which were confirmed by UPS and UV-vis spectroscopy. In particular, $BiVO_4/Ni_3(HHTP)_2$ had the highest photocurrent density of 4.66 mA cm^{-2}, which is 3.2 times greater than that of pristine $BiVO_4$. Among the three types of $M_3(HHTP)_2$, $Ni_3(HHTP)_2$ exhibited the highest bulk conductivity, indicating that the electrical conductivity of MOF and the type-II band alignment significantly influenced the photoelectrochemical performance. This study demonstrates that establishing a type-II heterojunction between semiconducting $M_3(HHTP)_2$ and $BiVO_4$ is a promising and general strategy for obtaining high-performance photoanodes.

Conflicts of interest

There are no conflicts to declare.

Acknowledgements

This work was supported by a grant from the Korea Environmental Industry & Technology Institute (No. 2020002700011).

Notes and references

1 Y. Li, L. Zhang, X. Xiang, D. Yan and F. Li, *J. Mater. Chem. A*, 2014, **2**, 13250–13258.
2 X. Cao, Y. Wang, J. Lin and Y. Ding, *J. Mater. Chem. A*, 2019, **7**, 6294–6303.
3 F. F. Abdi, T. J. Savenije, M. M. May, B. Dam and R. van de Krol, *J. Phys. Chem. Lett.*, 2013, **4**, 2752–2757.
4 L. Luo, Z.-j. Wang, X. Xiang, D. Yan and J. Ye, *ACS Catal.*, 2020, **10**, 4906–4913.
5 Z. Zhou, J. Chen, Q. Wang, X. Jiang and Y. Shen, *Chin. J. Catal.*, 2022, **43**, 433–441.
6 Z. Wang, Z. Lin, S. Shen, W. Zhong and S. Cao, *Chin. J. Catal.*, 2021, **42**, 710–730.
7 Y. Tang, R. Wang, Y. Yang, D. Yan and X. Xiang, *ACS Appl. Mater. Interfaces*, 2016, **8**, 19446–19455.
8 W. He, R. Wang, L. Zhang, J. Zhu, X. Xiang and F. Li, *J. Mater. Chem. A*, 2015, **3**, 17977–17982.
9 J. M. Lee, J. H. Baek, T. M. Gill, X. Shi, S. Lee, I. S. Cho, H. S. Jung and X. Zheng, *J. Mater. Chem. A*, 2019, **7**, 9019–9024.
10 J. Z. Su, L. J. Guo, N. Z. Bao and C. A. Grimes, *Nano Lett.*, 2011, **11**, 1928–1933.
11 M. Z. Xie, X. D. Fu, L. Q. Jing, P. Luan, Y. J. Feng and H. G. Fu, *Adv. Energy Mater.*, 2014, **4**, 1300995.
12 Q. G. Pan, C. Zhang, Y. J. Xiong, Q. X. Mi, D. D. Li, L. L. Zou, Q. H. Huang, Z. Q. Zou and H. Yang, *ACS Sustainable Chem. Eng.*, 2018, **6**, 6378–6387.
13 S. Q. Zhou, K. Y. Chen, J. W. Huang, L. Wang, M. Y. Zhang, B. Bai, H. Liu and Q. Z. Wang, *Appl. Catal., B*, 2020, **266**, 118513.
14 G. X. Liu, Y. P. Li, Y. Xiao, D. M. Jia, C. H. Li, J. J. Zheng and X. W. Liu, *Catal. Lett.*, 2019, **149**, 870–875.
15 C. H. Liu, H. Luo, Y. Xu, Z. H. Zhang, Q. Liang, W. C. Wang and Z. D. Chen, *Chem. Eng. J.*, 2020, **384**, 123333.

16 J. W. Yoon, J. H. Kim, C. Kim, H. W. Jang and J. H. Lee, *Adv. Energy Mater.*, 2021, **11**, 2003052.
17 T. Y. Chen, J. H. Dou, L. M. Yang, C. Y. Sun, N. J. Libretto, G. Skorupskii, J. T. Miller and M. Dinca, *J. Am. Chem. Soc.*, 2020, **142**, 12367–12373.
18 J. H. Kim, D. H. Kim, J. W. Yoon, Z. F. Dai and J. H. Lee, *ACS Appl. Energy Mater.*, 2019, **2**, 4535–4543.
19 J. A. Seabold and K. S. Choi, *J. Am. Chem. Soc.*, 2012, **134**, 2186–2192.
20 Y. Nonoguchi, D. Sato and T. Kawai, *Polymers*, 2018, **10**, 962.
21 K. W. Nam, S. S. Park, R. dos Reis, V. P. Dravid, H. Kim, C. A. Mirkin and J. F. Stoddart, *Nat. Commun.*, 2019, **10**, 4948.
22 W. H. Li, J. Q. Lv, Q. H. Li, J. F. Xie, N. Ogiwara, Y. Y. Huang, H. J. Jiang, H. Kitagawa, G. Xu and Y. B. Wang, *J. Mater. Chem. A*, 2019, **7**, 10431–10438.
23 S. C. Wang, P. Chen, Y. Bai, J. H. Yun, G. Liu and L. Z. Wang, *Adv. Mater.*, 2018, **30**, 1800486.
24 Q. Qin, Q. Cai, W. T. Hong, C. Y. Jian and W. Liu, *Chem. Eng. J.*, 2020, **402**, 126227.
25 M. Fang, Q. A. Cai, Q. Qin, W. T. Hong and W. Liu, *Chem. Eng. J.*, 2021, **421**, 127796.
26 J. Li, F. Li and J. Jin, *J. Power Sources*, 2021, **482**, 228957.
27 J. Jian, Y. Xu, X. Yang, W. Liu, M. Fu, H. Yu, F. Xu, F. Feng, L. Jia, D. Fredich, R. van de Krol and H. Wang, *Nat. Commun.*, 2019, **10**, 2609.
28 Y. M. Jo, K. Lim, J. W. Yoon, Y. K. Jo, Y. K. Moon, H. W. Jang and J. H. Lee, *ACS Cent. Sci.*, 2021, **7**, 1176–1182.
29 L. S. Xie, G. Skorupskii and M. Dinca, *Chem. Rev.*, 2020, **120**, 8536–8580.
30 D. Sheberla, L. Sun, M. A. Blood-Forsythe, S. Er, C. R. Wade, C. K. Brozek, A. Aspuru-Guzik and M. Dinca, *J. Mater. Chem. A*, 2014, **136**, 8859–8862.
31 M. Hmadeh, Z. Lu, Z. Liu, F. Gandara, H. Furukawa, S. Wan, V. Augustyn, R. Chang, L. Liao, F. Zhou, E. Perre, V. Ozolins, K. Suenaga, X. F. Duan, B. Dunn, Y. Yamamto, O. Terasaki and O. M. Yaghi, *Chem. Mater.*, 2012, **24**, 3511–3513.
32 R. Dong, P. Han, H. Arora, M. Ballabio, M. Karakus, Z. Zhang, C. Shekhar, P. Adler, P. S. Petkov, A. Erbe, S. C. B. Mannsfeld, C. Felser, T. Heine, M. Bonn, X. L. Feng and E. Canovas, *Nat. Mater.*, 2018, **17**, 1027.
33 X. Huang, P. Sheng, Z. Y. Tu, F. J. Zhang, J. H. Wang, H. Geng, Y. Zou, C. A. Di, Y. P. Yi, Y. M. Sun, W. Xu and D. B. Zhu, *Nat. Commun.*, 2015, **6**, 7408.
34 A. H. Wilson, *Proc. R. Soc. London*, 1938, **167**, 0580–0593.
35 M. L. O. Ne, M. Boujnah, A. Benyoussef and A. El Kenz, *J. Supercond. Novel Magn.*, 2017, **30**, 1263–1267.
36 M. E. Foster, K. Sohlberg, C. D. Spataru and M. D. Allendorf, *J. Phys. Chem. C*, 2016, **120**, 15001–15008.
37 H. Dotan, K. Sivula, M. Gratzel, A. Rothschild and S. C. Warren, *Energy Environ. Sci.*, 2011, **4**, 958–964.
38 D. K. Zhong, S. Choi and D. R. Gamelin, *J. Am. Chem. Soc.*, 2011, **133**, 18370–18377.
39 P. M. Rao, L. L. Cai, C. Liu, I. S. Cho, C. H. Lee, J. M. Weisse, P. D. Yang and X. L. Zheng, *Nano Lett.*, 2014, **14**, 1099–1105.